Yisheng Liu ✉
Shuqi Zhou
Xufeng Sun

https://doi.org/10.21278/TOF.484061323
ISSN 1333-1124
eISSN 1849-1391

RESEARCH ON THE MOTION MECHANISM OF YARNS WITH DIFFERENT LENGTHS IN A PNEUMATIC TUCKED-IN SELVEDGE AIRFLOW FIELD

Summary

Due to the requirements of the textile industry for high-speed weaving of looms, pneumatic tucked-in selvedge apparatus is being adopted by more and more shuttleless looms. In this paper, the fluid–structure interaction method is used to analyse and simulate the motion law of yarns with different lengths in the pneumatic tucked-in selvedge apparatus and its influence on the yarn tucked in. Then, the yarn movement is recorded by a high-speed camera, and the collected experimental information is compared with the simulation results and analysed. The results provide theoretical support for improving the quality of the yarn tucked in and the efficiency in the pneumatic tucked-in selvedge apparatus.

Key words: *Yarn, fluid–structure interaction (FSI), pneumatic tucked-in selvedge apparatus, oblique-blowing airflow, folding-in airflow*

1. Introduction

In the textile industry, shuttleless looms are widely used because of their high efficiency. However, due to their special weft insertion characteristics, it is impossible to form a smooth edge in the knitting process. In order to solve the problem of raw edges formed by shuttleless looms, different kinds of tucked-in selvedge apparatus have been invented. As an important type of tucked-in selvedge apparatus, a pneumatic tucked-in selvedge apparatus has been greatly popularized in recent years thanks to the in-depth research of predecessors.

In recent years, researchers have widely used the fluid–structure interaction (FSI) algorithm to simulate the movement of fibre or yarn in the airflow field and study its spatial movement law in the airflow field. De Meulemeester et al. [1] established a one-dimensional mathematical model of yarn, and used Newton's second law to describe the behaviour of yarn. They put forward a three-dimensional model of yarn on the basis of their one-dimensional model. Delcour et al. [2] carried out a three-dimensional fluid-solid coupling simulation of the yarn under the action of the main nozzle airflow of the air-jet loom and discussed the feasibility of using the Chimera technology to simulate the interaction between the yarn movement and the main nozzle airflow. Guo et al. [3] pointed out that the standard k-ε two-equation turbulence model ignored the anisotropic viscosity caused by the streamline curvature effect and the

generation of extra turbulence, so they adopted an achievable k-ε turbulence model to simulate the flow characteristics in the slotted tube nozzle. This model is an eddy viscosity model, which consists of a new model dissipation rate equation and a new realizable eddy viscosity formula proposed by Shih et al. [4]. Ahmed et al. [5] established a computational fluid dynamics model to simulate the air flow behaviour inside the air nozzle and used it to study, analyse, predict, and control the influence of the rotating air flow behaviour on the fibre movement and yarn properties. Osman et al. [6] considered the interaction between air flow and yarn and used a three-dimensional, two-way fluid–structure interaction model to simulate the deformation wave of free yarn clamping on one side. In the research, the yarn is simulated as a flexible cylinder, and the arbitrary Lagrangian-Euler technique is adopted. The simulation results are compared with the experiments quantitatively and qualitatively.

At present, a numerical research method based on the combination of the immersed boundary method (IBM) and the lattice Boltzmann method (LBM) is widely used to study the dynamic behaviour of fluid–structure interaction between yarn or fibre and the air flow field, which is also the latest research result in this field. Tian et al. [7] combined the submerged boundary method with the lattice Boltzmann method to simulate the hydrodynamic interaction of elastic wires and determined that the immersed boundary lattice Boltzmann method (IB-LBM) has excellent computational simulation efficiency for a class of fluid–solid structure interaction problems that need to solve the details of the process model. Cui et al. [8] numerically simulated the fluid–fibre interaction of a single flexible fibre in the fibre transmission channel based on the momentum exchange immersed boundary lattice Boltzmann algorithm (IB-LBM), which proved that this algorithm can effectively simulate the interaction between fluid and flexible body involving large deformation. Although the above-mentioned research is helpful in simulating and analysing the interaction between yarn and the airflow field, there is no three-dimensional simulation analysis of the behaviour of yarns with different lengths in the airflow.

However, the structural requirements, such as a high aspect ratio of fibre or yarn, certain flexibility, and interaction when a contact occurs, have posed great challenges to the modelling stage of numerical simulation. Li et al. [9] modelled the yarn path as a series of two-node beam elements when simulating the yarn bent by a braided rope bundle and determined the path of the braided yarn through a single parameter. Deng et al. [10] developed a yarn-level parametric modelling method based on the Rhino Grasshopper approach. By analysing the geometric and structural characteristics of fibre and spinning the cross-sectional shape, the stacking distribution and yarn hairiness are established, thus establishing a three-dimensional yarn model. Kaldor et al. [11] defined a knitting calculation model that simulated the yarn as an inextensible curve with bending resistance. Kondora and Asendych [12] simulate the movement of fibres by representing them as chains of elements connected together. Zhou et al. [13] regard flexible filament as a digital chain connected by a series of rod elements and choose elastic rod elements to simplify the model in finite element analysis.

In this paper, the interaction between yarn and the pneumatic tucked-in selvedge apparatus is considered and explored in three dimensions. In this study, focusing on the yarn tucked in, the macroscopic fluid model of airflow field and the finite element yarn solid model are established in turn based on the one-way fluid–structure weak interaction algorithm, and the complete process from the obliquely blown to the folding-in yarns with different lengths is numerically simulated and explored by visual experiments. The main research focus of this paper is the burrs with different lengths of yarn after weft insertion. It can complete the tucking-in process and form the tucked-in effect under the action of airflow. During this process, the burrs stretch slightly, which can affect the selvedge of the finished fabric at a certain level. The

faster the burr is tucked in, the better the tucked-in effect of the burr is, the firmer the selvedge of the finished fabric is, and the harder it is to collapse and break it. However, the shorter the yarn burr is, the smaller the elongation of the burr is, the lower the tightness of the burr tucked in is, and the less compact and beautiful it is. The elongation of the yarn can be controlled by varying and optimizing the length of the yarn burr. Through simulation and experiment, we can find the best advantage of the length of yarn burr according to actual conditions, which can meet the requirements of fast tucking in, good tucked-in effect, firm selvedge of the finished fabric, proper hairiness, tight burr, and compact and beautiful appearance. The results can provide a theoretical basis for the subsequent optimization of the pneumatic tucked-in selvedge apparatus.

2. Numerical simulation

Fluid–structure interaction (FSI) refers to the interaction between fluid and solid, which leads to a series of phenomena related to system motion [14-15]. In this paper, the spatial motion of a single solid yarn with one end fixed and the other end free in a pneumatic tucked-in airflow field is studied. Since a single yarn has little effect on the airflow field data, a weak coupling algorithm can be used to separate the airflow field from the yarn, and the calculated airflow field fluid data can be converted into aerodynamic force and transmitted to the grid nodes of the yarn. Therefore, the one-way fluid-structure coupling algorithm is used. There is no need to re-grid multiple times during iteration, and the calculation amount can be greatly reduced and the convergence can be faster.

2.1 Fluid model of airflow field

The three-dimensional geometric model of a loom pneumatic tucked-in selvedge testing apparatus with adjustable spatial multi-parameters constructed in this paper is shown in Fig. 1 (a), in which the gas pipeline includes four parts, namely three air inlet pipes, one holding pipe, one oblique-blowing pipe, and four folding-in pipes. When the airflow in the air compressor is ejected from the end of the oblique-blowing pipe and the folding-in pipe, the airflow is still at a high speed. The boundary conditions of the 3D flow field model are the non-slip boundary conditions, all the airflow hole walls (Wall) are set as non-slip boundary wall surface conditions, and the rest (Outlet) are set as pressure outlet conditions. In order to set the static pressure boundary conditions of the fluid field of the fluid model of the airflow field more conveniently, accurately, and effectively, a fluid calculation field of 21 mm * 38 mm * 20 mm is further expanded on the basis of the original three-dimensional geometric model. Inlet 1 and Inlet 2 comprise respectively the inlet of an oblique-blowing air inlet pipe and the inlet of folding-in air inlet pipe. Inlet 3 comprises the inlet of holding air inlet pipe. The walls of all flow field fluid model pipes are classified as the Wall, and the other surfaces are classified as the Outlet. Then the structured tetrahedron grid is used to mesh the fluid model of the airflow field; the maximum mesh size of the entire watershed is 0.8 mm. Inlet 1, Inlet 2, Inlet 3, and the Wall are all meshed with refinement. The maximum grid size of Inlet 1, Inlet 2, and Inlet 3 is 0.1mm, containing 6956, 6970, and 6947 units, respectively. The maximum grid size of the Wall is 0.5 mm, containing 39076 units. The Outlet and the body contain 42,320 and 1,794,421 elements, respectively, and the model contains a total of 1,896,690 elements and 345,122 nodes, as shown in Fig. 1(b).

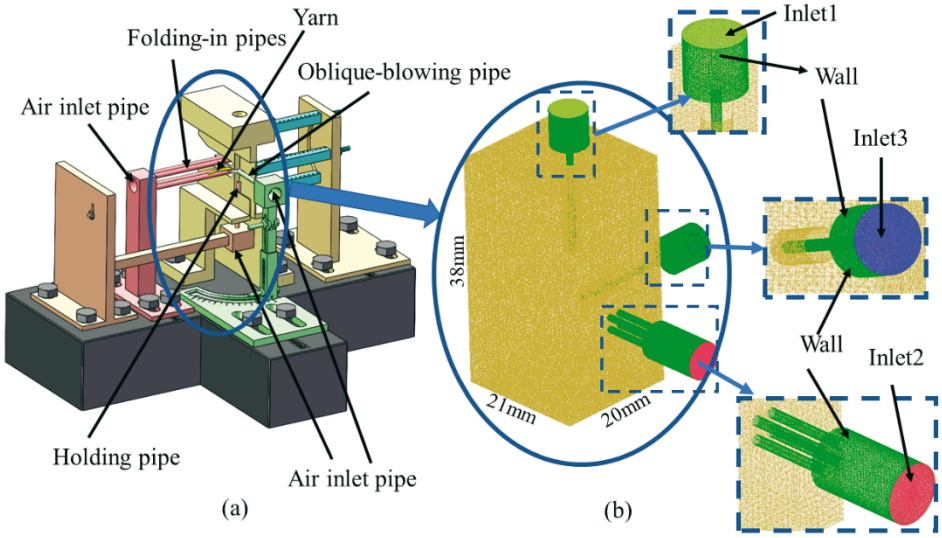

Fig. 1 A 3D geometric model of the pneumatic tucked-in selvedge apparatus

2.2 CFD solution mode and control equation

The basic equations of fluid mechanics (continuity equation, motion equation, energy equation, and state equation [16]) must be satisfied when the air flows in the pipeline of the pneumatic tucked-in selvedge apparatus or is sprayed to the working area of the pneumatic tucked-in selvedge apparatus. In addition, due to the relationship between the radius of the air inlet pipe and the oblique-blowing pipe, the velocity of the airflow at the junction of the air inlet pipe and the oblique-blowing pipe is extremely high, so that the Reynolds number is as high as 1.7×10^4 based on the Reynolds number formula. Therefore, the fluid phase simulated in this paper is assumed to be a three-dimensional compressible and stable viscous turbulent flow, and the gas flow in the pipeline and the working area of the pneumatic tucked-in selvedge apparatus belongs to a turbulent flow. At present, there are three main methods to solve the CFD problem of fluid turbulent flow: 1. Direct numerical simulation (DNS) for simulating low Reynolds numbers (about 200); 2. Large eddy simulation (LES), which consumes a lot of computing resources while its application is not yet mature; 3. The Reynolds averaged Navier-Stokes (RANS) method, which is solved by the Reynolds averaged N-S equations.

Among the three methods listed above, the Reynolds averaged Navier-Stokes method is used in this paper as the most suitable [17-18]. In addition, referring to Shih's research, it is found that the effect of a standard k-ε model in simulating the flow in the pipeline is much less strong than that of a realizable k-ε turbulence model, so it is more practical to use the realizable k-ε model to simulate the flow in the airflow field in this paper [4].

According to the law of conservation of mass, the expression in vector form of the fluid continuity equation per unit mass can be written as:

$$\frac{\partial\rho}{\partial t}+\frac{\partial\left(\rho u_j\right)}{\partial x_j}=0\,, \tag{1}$$

where ρ is the air density, t is the time, $u_j\left(i=x,y,z\right)$ and $x_j\left(i=x,y,z\right)$ are the velocity component and the displacement component in three directions, respectively.

According to the law of conservation of momentum, the expression in vector form of the equation of motion of a fluid per unit mass is given by:

$$\frac{\partial(\rho u_i)}{\partial t}+\frac{\partial(\rho u_i u_j)}{\partial x_j}=\rho f_i-\frac{\partial p}{\partial x_i}-\frac{\partial}{\partial x_i}\left(\frac{2}{3}\mu\frac{\partial u_i}{\partial x_j}\right)+\frac{\partial}{\partial x_j}\left[\mu\left(\frac{\partial u_i}{\partial x_j}+\frac{\partial u_j}{\partial x_i}\right)\right] \tag{2}$$

According to the law of conservation of energy, the expression of the energy conservation equation is specified by:

$$\frac{\partial}{\partial t}\left[\rho\left(e+\frac{u_i^2}{2}\right)\right]+\frac{\partial}{\partial x_j}\left[\rho\left(e+\frac{u_i^2}{2}\right)u_j\right]=\dot{\rho q}+\rho f_j u_j-\frac{\partial p u_j}{\partial x_j}+\frac{\partial \tau_{ji}u_i}{\partial x_j}+\frac{\partial}{\partial x_j}\left(C_p\frac{\mu}{\mathrm{Pr}}\frac{\partial T}{\partial x_j}\right) \tag{3}$$

In the formula, where μ is the dynamic viscosity coefficient, τ_{ji} is the viscous stress tensor component, $x_i\,(i=x,y,z)$ represents the displacement components in the three coordinate directions, $u_i\,(i=x,y,z)$ denotes the velocity components in the three coordinate directions, f_i, e, q, C_p, Pr, and T are the stress component, internal energy, heat flux, heat capacity, Prandtl number, and temperature, respectively.

The basic equations of flow have six independent variables, but only five equations are provided. They are not completely closed, so it is necessary to add a state equation to close them. The three-dimensional compressible and stable viscous turbulent airflow (air) numerically simulated in this paper can be regarded as an ideal gas, so the expression of the equation of state can be written as:

$$\mathrm{p}=\mathrm{R}\rho T=(\gamma\text{-}1)\rho \mathrm{e}\,, \tag{4}$$

where R is the molar gas constant.

2.3 Yarn finite element model

In the numerical simulation carried out in this paper, the displacement, deformation, and mutual contact of yarns need to be considered; therefore, the yarn with one end fixed and the other end free will be affected by axial force, bending moment, and torque when it is in the pneumatic tucked-in airflow field [19-20]. In this paper, it is found that neither the bar element nor the truss element is suitable for constructing a yarn solid model. Consequently, an attempt to construct the yarn solid model with the beam element is made resulting in success after extensive exploration. Therefore, the spatial elastic beam element (BEAM) is selected and simplified in the finite element analysis software ABAQUS, and the yarn solid model is discretized into a digital chain [21] composed of continuous elastic spatial beam elements; thus, the yarn solid model is successfully constructed. Because the finite element method is adopted in the process, the model is called the yarn finite element model, as shown in Fig. 2.

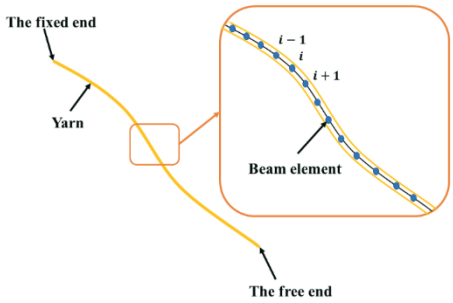

Fig. 2 Elastic beam model of yarn

2.4 Fluid-structure interaction algorithm

The coupling algorithm is an important link in information exchange among multiple physical fields [22-26]. The one-way fluid–structure weak interaction algorithm proposed in this paper can simultaneously solve the problems of two physical field data: the pneumatic tucked-in airflow field and the yarn solid field. In this paper, the fluid data of yarn at each time step is converted into the corresponding aerodynamic force in real time by using the one-way fluid–structure weak coupling algorithm and transmitted to the nodes of the space elastic beam element of solid yarn. Then, the iterative algorithm is used to calculate the displacement, deformation, and aerodynamic force in real time, and the numerical simulation of the whole oblique blowing and folding-in process of yarn in the pneumatic tucked-in air field can be realized. Thus, firstly, the fluid data of the flow field of the node of the yarn elastic beam unit needs to be extracted. Because the overlap between the fluid model unit of the airflow field and the yarn solid model unit is small, it is impossible to achieve a one-to-one matching relationship; therefore, the fluid data of the corresponding yarn solid unit node cannot be obtained directly from the fluid data of the fluid model unit node of the airflow field, as shown in Fig. 3(a).

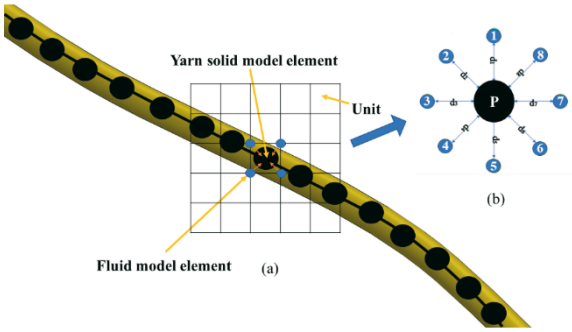

Fig. 3 Schematic diagram of the inverse distance- weighted interpolation algorithm

Fortunately, there is a strong correlation between the fluid data in the region. The inverse distance-weighted interpolation algorithm can be used to calculate the unknown fluid data on the yarn beam unit nodes in a certain range according to the known fluid data of the air flow field fluid model unit nodes, and the fluid data of all yarn solid unit nodes can be successfully extracted, as shown in Fig. 3(b). The airflow field data of any element node in the airflow field can be calculated using the following formula [27, 28]:

$$Z_p = \sum_{i=1}^{n} \lambda_i Z_i \tag{5}$$

$$\lambda_i = \frac{d_i^{-k}}{\sum_{i=1}^{n} d_i^{-k}}, \tag{6}$$

where Z_p is the estimated value of the flow field data of the node P to be interpolated, Z_i represents the flow field data value of the i-th grid sampling point, λ_i and d_i are the weight and distance from the i-th grid sample point to the node to be interpolated, respectively, n is the number of grid sample points participating in the calculation, and k denotes the power exponent.

Then, the Buckingham $\prod$ theorem is applied to convert the extracted fluid data into aerodynamic forces on each unit node. The magnitude of aerodynamic force (F) is mainly influenced by three factors: airflow density (ρ), relative movement speed between airflow and yarn (v), and contact area (A).Therefore, according to the Buckingham $\prod$ theorem, it can be deduced that the relationship between the four quantities can be written as [29, 30]:

$$\Pi=\rho^{-1}v^{-2}A^{-1}F=\frac{\mathrm{F}}{\rho v^{2}A} \tag{7}$$

According to the engineering experience, the value of $\prod$ derived from the Buckingham $\prod$ theorem is related to the gas resistance coefficient (C_d), and its value is 1/2 the value of the gas resistance coefficient (C_d). Moreover, the aerodynamic force (F) can be decomposed along the axial direction and radial direction of the yarn, as shown in Fig. 4, and the following results can be obtained:

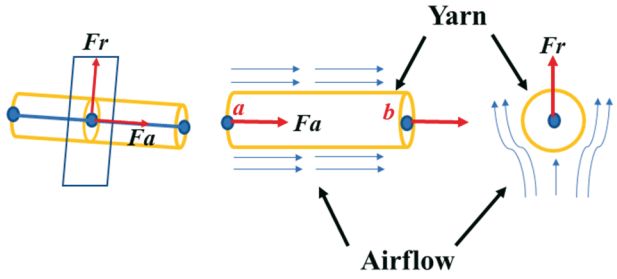

Fig. 4 A schematic diagram of aerodynamic force decomposition

$$F_a=\frac{1}{2}C_a\rho s_a\left|v_a\right|v_a=\frac{1}{2}C_a\rho\pi dl\left\|v_a\right\|v_a \tag{8}$$

$$F_r=\frac{1}{2}C_r\rho s_r\left|v_r\right|v_r=\frac{1}{2}C_r\rho\pi rl\left\|v_r\right\|v_r \tag{9}$$

$$v_a=v\cdot r_{ab},v_r=v-v_a, \tag{10}$$

where C_a and C_r are the axial and radial resistance coefficients of the yarn, respectively, s_a is the windward area of the yarn, s_r is the cross-sectional area of the yarn, r_{ab} is the displacement vector composed of two nodes of the decomposition unit, v_a and v_r are the axial and radial relative motion velocities of the yarn and airflow, respectively. The empirical formulas of the axial and radial resistance coefficients of cotton yarn are obtained by fitting through many experiments; they can be expressed as:

$$\mathrm{C}_a=0.8945\cdot\left|v\right|^{-0.6854} \tag{11}$$

$$\mathrm{C}_r=4.8246\cdot\left|v\right|^{-0.5254} \tag{12}$$

Finally, the displacement of the yarn unit node is calculated by an explicit dynamic algorithm. The explicit kinetics algorithm is an explicit algorithm based on the kinetic equation, calculating the state at the end of the post-increment step from the known state at the end of the pre-increment step. The dynamic equilibrium equation of the yarn solid model node is given by:

$$a_{(t)}=\frac{P_{(t)}}{M}-\frac{I_{(t)}}{M}, \tag{13}$$

where $a_{(t)}$ is the acceleration at a certain time, M is the node mass matrix, $P_{(t)}$ and $I_{(t)}$ are the external and internal forces at a node at a certain time, respectively.

3. Numerical simulation results and analysis

In the numerical simulation, the movement of the yarn can be divided into two stable equilibrium stages: the first stage is the movement of the yarn under the action of the oblique - blowing airflow; the second stage is the movement of the yarn under the action of the folding-in airflow.

In FLUENT**,** the relative air pressure of inlet 1 with oblique-blowing air is at first 0.04 MPa, and the relative air pressure of inlet 2 with folding-in air is 0 MPa. Obviously, there is no folding-in airflow condition. The oblique-blowing airflow with an initial air pressure of 0.04 MPa is vertically injected into the pneumatic tucked-in airflow field at a high speed; this affects the state of the airflow field around it, including the speed and pressure of the airflow field, and causes the fluctuation of the airflow field. The nephogram of velocity and pressure distribution of oblique-blowing airflow is shown in Figs. 5(a) and (b).

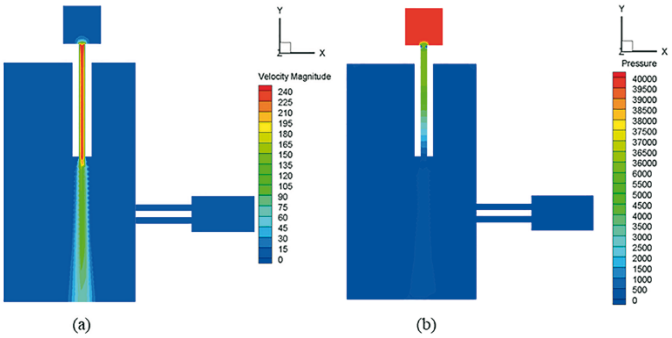

Fig. 5 The nephogram of velocity and pressure distribution in oblique-blowing airflow

Then, a change in the settings in FLUENT is made: the relative air pressure of inlet 1 of oblique-blowing air is reduced to 0 MPa, and the relative air pressure of inlet 2 of folding-in air is changed into 0.04 MPa. Thus, there is no oblique-blowing airflow condition. The folding-in airflow with an initial air pressure of 0.04 MPa is injected horizontally into the pneumatic folded airflow field at a high speed, which affects the state of the airflow field around it and causes the fluctuation of the airflow field. The nephogram of the velocity and pressure distribution of the folding-in airflow is shown in Figs. 6(a) and (b).

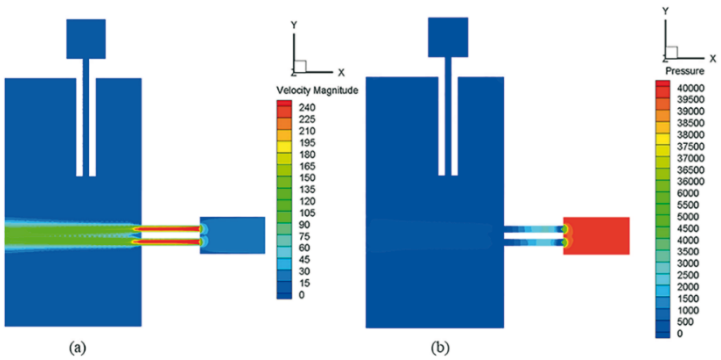

Fig. 6 The nephogram of the velocity and pressure distribution of the folding-in airflow

If we compare the action stage of the oblique-blowing airflow and that of the folding-in airflow, the difference is that the folding-in airflow is horizontally injected into an unbound area through four folding-in pipes arranged neatly and orderly, while the oblique-blowing airflow is vertically injected through only one oblique-blowing pipe. As a result, the velocity and pressure states of the folding-in airflow are more stable than those of the oblique-blowing airflow.

In this paper, four kinds of yarns with lengths of 8 mm, 10 mm, 12 mm, and 15 mm are selected to explore the influence of yarns with different lengths on yarn tucked in in a pneumatic tucked-in selvedge apparatus. In the numerical simulation results, the 3D motion state and final equilibrium state of yarns with four different lengths in the pneumatic tucked-in airflow field are selected, as shown in Fig. 7. Figures 7 (a) and (b) show the oblique-blowing and folding-in motion states of yarns, respectively.

At the beginning, yarns of four different lengths are all in a horizontal position, forming a straight line, as shown in Fig. 7(a). After the oblique-blowing airflow affects the airflow field, the front part of the yarn begins to move in the negative direction of the Y-axis under the action of the oblique-blowing airflow, and the whole yarn presents an approximate V-shaped oblique-blowing motion state. Gradually, the front section of the yarn moves in the negative Y-axis direction, and the free end of the yarn also moves in the negative Y-axis direction along with the front section. As a result, the entire yarn exhibits an approximately U-shaped oblique-blowing motion state. With the continuous action of oblique-blowing airflow, the free end of the yarn gradually moves in the negative direction of the X-axis, eventually reaching the oblique-blowing balance state, and the whole yarn presents an approximate "1"-shaped oblique-blowing motion state. The longer the yarn length, the longer it takes to complete the whole oblique-blowing process. From Table 1, one can conclude that the yarn will be slightly elongated during the whole oblique-blowing process, and its elongation will increase with an increase in the yarn length. The aerodynamic force becomes smaller with the distance from the inclined, oblique-blowing pipes, but the influence range becomes larger.

After the yarn is in the oblique-blowing equilibrium state under the action of oblique-blowing airflow, the folding-in airflow enters the pneumatic tucked-in airflow field, which affects the state of the yarn in the oblique-blowing equilibrium state and causes the spatial movement of the yarn folding-in process. As can be seen from Fig. 7(b), the middle and rear parts of the yarn that have reached the oblique-blowing equilibrium state under the action of oblique-blowing airflow move in the negative direction of the X-axis under the action of folding-in airflow. Under the continuous action of the folding-in airflow, the free end of the yarn moves in the negative direction of the X-axis and gradually moves in the positive direction of the Y-axis, finally completing the folding-in process and reaching the folding-in state. From Table 2, one can see that during the whole folding-in process, the yarn will stretch first and then shrink, and the aerodynamic force will change slightly with the distance from the folding-in pipes, and the influence range will gradually increase.

From the simulation of the whole oblique blowing-folding process, one can conclude that with an increase in the yarn length, the time for a yarn to complete the oblique-blowing and folding-in processes will also increase greatly, and the time required for the tucked-in yarn of 12 mm is 11.05 ms longer than that of 8 mm. Due to inertia and other yarn-related reasons, the time required for the oblique-blowing process is always longer than the time required for the folding-in. In addition, as the yarn is elastic and stretchable, it will exhibit a process of contraction after stretching under the action of aerodynamic force.

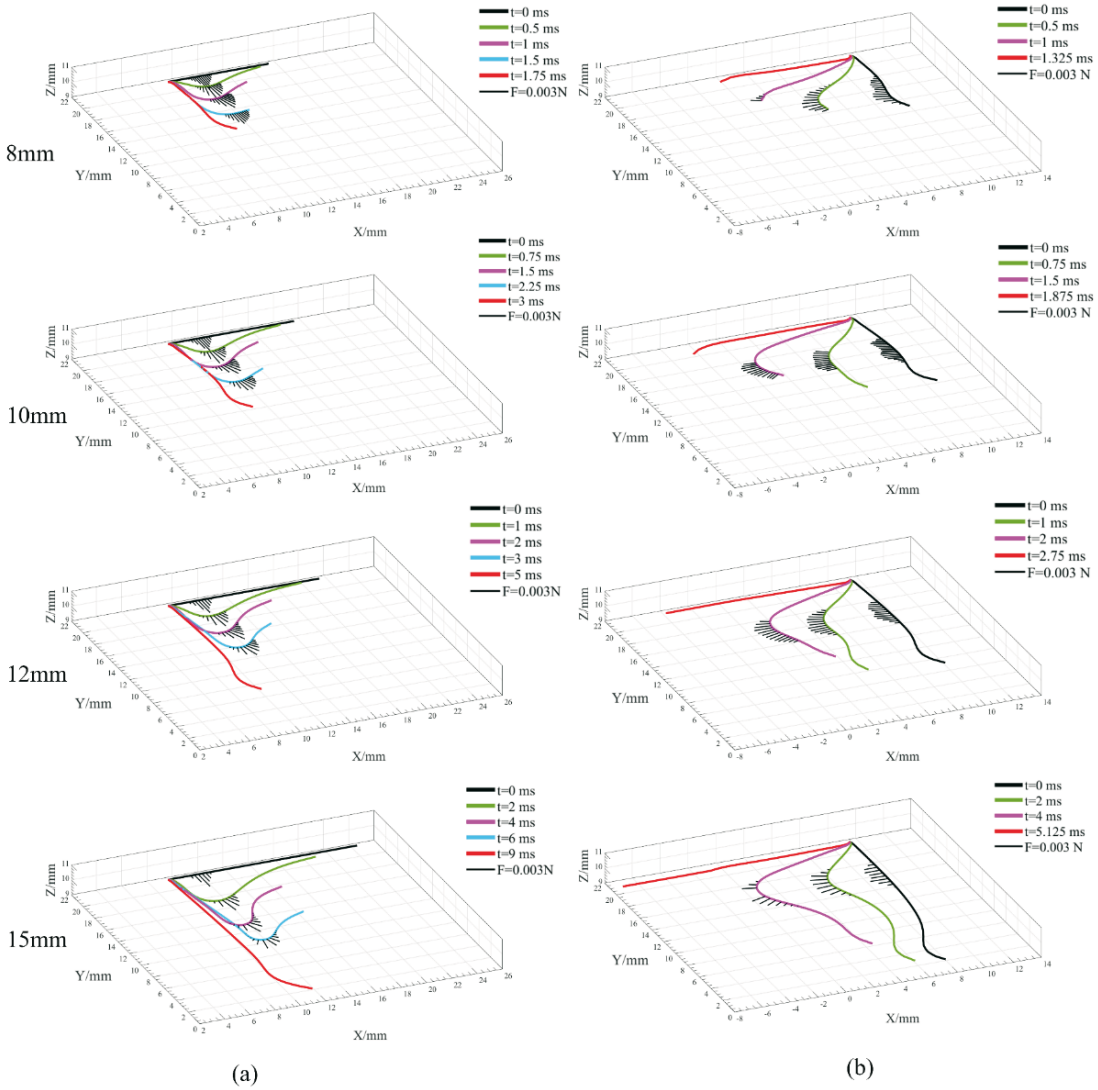

Fig. 7 Trajectory motion diagram of yarns with four lengths

Table 1 Length of yarn in the oblique-blowing process and the aerodynamic force of the beam element node with X = 12.5 mm

8 mm yarn	t = 0 ms	t = 0.5 ms	t = 1 ms	t = 1.5 ms	t = 1.75 ms
Length (mm)	8.000	8.146	8.345	8.683	8.952
Aerodynamic force (mN)	4.18	3.94	3.42	2.91	/
10 mm yarn	t = 0 ms	t = 0.75 ms	t = 1.5 ms	t = 2.25 ms	t = 3 ms
Length (mm)	10.000	10.233	10.500	10.936	11.657
Aerodynamic force (mN)	4.18	3.74	2.72	2.38	/
12 mm yarn	t = 0 ms	t = 1 ms	t = 2 ms	t = 3 ms	t = 5 ms
Length (mm)	12.000	12.312	12.640	13.126	14.741
Aerodynamic force (mN)	4.18	3.38	2.47	2.19	/
15 mm yarn	t = 0 ms	t = 2 ms	t = 4 ms	t = 6 ms	t = 9 ms
Length (mm)	15.000	15.603	16.333	17.402	19.797
Aerodynamic force (mN)	4.18	3.25	2.36	1.87	/

Table 2 Length of yarn in the folding-in process and the aerodynamic force of the beam element node with Y = 13.95 mm

8 mm yarn	t = 0 ms	t = 0.5 ms	t = 1 ms	t = 1.325 ms
Length (mm)	8.952	9.216	8.861	8.564
Aerodynamic force (mN)	1.64	1.61	0.31	/
10 mm yarn	t = 0 ms	t = 0.75 ms	t = 1.5 ms	t = 1.875 ms
Length (mm)	11.657	11.989	10.936	10.523
Aerodynamic force (mN)	1.64	1.57	1.31	/
12 mm yarn	t = 0 ms	t = 1 ms	t = 2 ms	t = 2.75 ms
Length (mm)	14.741	14.915	14.349	14.126
Aerodynamic force (mN)	1.64	1.41	1.25	/
15 mm yarn	t = 0 ms	t = 2 ms	t = 4 ms	t = 5.125 ms
Length (mm)	19.797	19.603	18.951	18.257
Aerodynamic force (mN)	1.64	1.39	1.07	/

4. Visual experiment

In order to verify the one-way fluid–structure weak interaction algorithm and explore the length of yarn that affects the spatial motion of the yarn, a pneumatic tucked-in selvedge apparatus was designed, and a visual experimental platform including a high-speed camera was built. The camera can capture and record the spatial movement of the yarn in real time, as shown in Fig. 8(b). The experimental platform mainly included two parts: a gas circuit and a circuit. The working principle diagram is shown in Fig. 8(a).

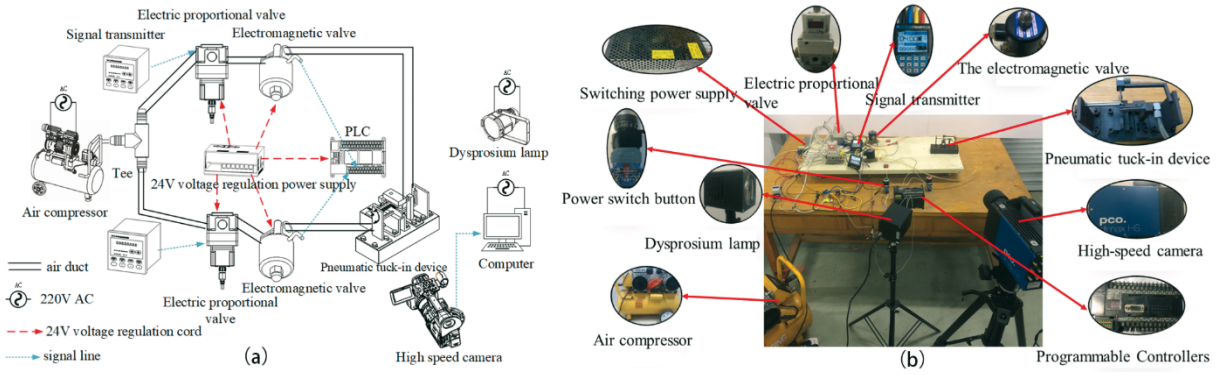

Fig. 8 Working principle schematic diagram (a) and experimental bench (b)

In this experiment, the motion of yarns with different lengths under the action of oblique-blowing and folding-in airflows was studied. According to the previous simulation research, four groups of yarns with different lengths were selected. The other conditions of the four groups of yarns were the same, except the yarn length changed; it was 8 mm in group A, 10 mm in group B, 12 mm in group C, and 15 mm in group D. The movement of the yarn was then recorded with a high-speed camera at a speed of 5469 frames per second, with a size of 1400*1050.

In the experiment with the yarn tucked in by a pneumatic selvedge apparatus, ordinary pure cotton yarn was selected as the object of research. The basic physical parameters of the yarn were determined through experimental tests. The weight of a 100-meter-long pure cotton yarn was measured to be 5.5 g, and the average diameter of cotton yarn was 0.38 mm. A high-precision balance and an electron microscope were used for measurements. According to the density formula, the yarn density of this model is 485 kg/m^3. The values of yarn density, diameter, Young's modulus, and Poisson's ratio are shown in Table 3.

Table 3 Material parameters of the yarn solid model

Yarn type	Density (kg/m3)	Diameter (mm)	Young's modulus (MPa)	Poisson's ratio
Cotton yarn	485	0.38	80	0.3

Since the direction of the oblique-blowing and folding-in airflow is perpendicular to the direction of its gravity, its gravity is also much smaller than the aerodynamic force. In addition, the appropriate holding airflow is utilized to offset the influence of gravity on the yarn in the experiments. Therefore, the influence of gravity is neglected in order to reduce computational complexity in CFD numerical simulations.

The details of the air pipe settings are shown in Fig. 9. The angle between the oblique-blowing pipe and the folding-in pipes was 90 degrees, the diameter of the oblique-blowing pipe was 1 mm, the nozzle of the oblique-blowing pipe was 4 mm away from the yarn, and the centre of the oblique-blowing pipe was offset from the fixed end of the yarn to the free end by 2.5 mm. Similarly, the incident angle of the four folding-in pipes was 0°, the diameter of the four folding-in pipes was 1mm, and the nozzle of the four folding-in pipes was 5mm from the yarn.

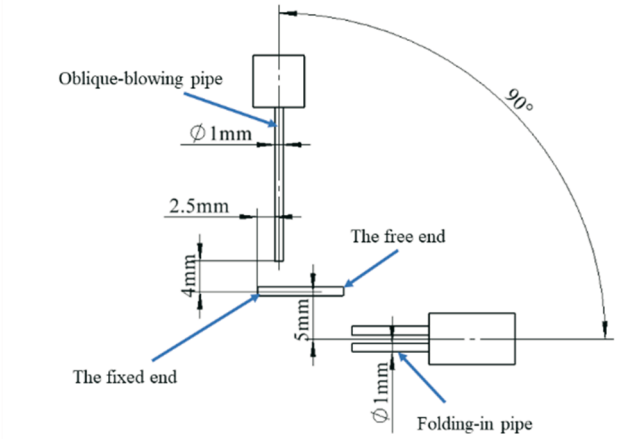

Fig. 9 Air pipe setting diagram

To further explore the influence of the length of yarn on the yarn tucked-in effect and verify the numerical simulation results, a large number of experiments were carried out on yarn oblique-blowing and folding-in. From the numerical simulation results shown in Fig. 7, it can be inferred that when the yarn length is more than 15mm, the yarn tucked-in time will be greatly prolonged until the airflow cannot push the yarn end to move, resulting in yarn tucked-in failure. Therefore, in this paper, only yarns with lengths of 8, 10, 12, and 15mm are compared and analysed. The experimental results are shown in Fig. 10. Figures10 (a), (b), (c), and (d) show the three-dimensional state changes of the yarn when the yarn length is 8, 10, 12, and 15 mm, respectively. Table 4 shows the time and elongation of yarn in experiment and simulation.

Based on Fig. 10, it can be seen that yarns of10 mm, 12 mm, and 15 mm can be tucked in, but in the experiment with 8 mm yarns, the force exerted by the folding-in airflow cannot resist the rebound force caused by the bending stiffness of the yarn, which leads to the failure of 8 mm yarns to be completely tucked-in. It also can be seen from the figure that the longer the yarn is, the easier it is to be bent by airflow, and when the airflow acts on the yarn at the beginning, the amplitude of the generated bow shape is larger, and the final tucked-in effect is better. Based on Table 4, it is found that the oblique-blowing time of the yarn is basically longer than the folding-in time; the longer the length of the yarn, the longer the time it takes to tucks and the longer the yarn becomes after having been tucked in.

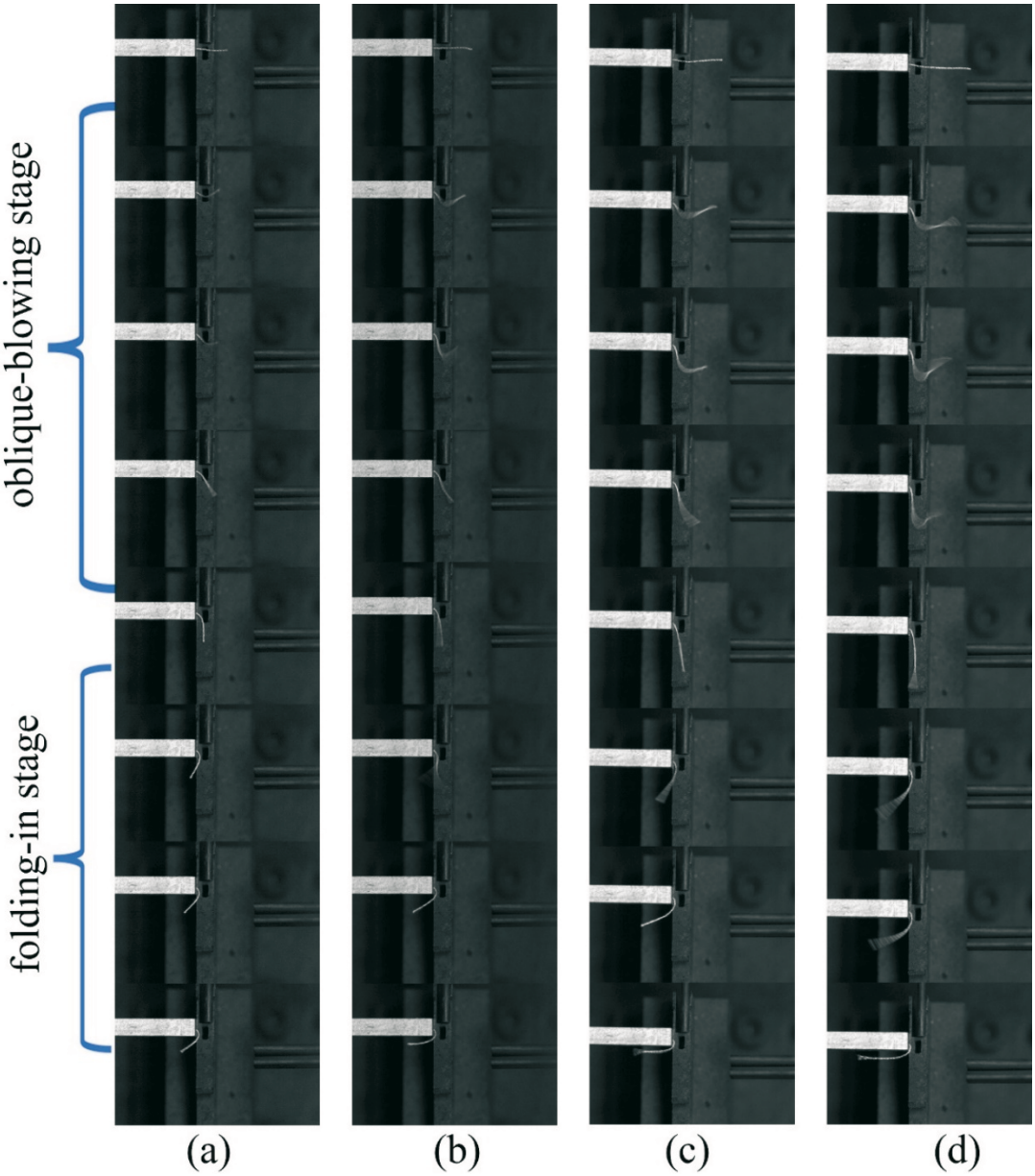

Fig. 10 Trajectory of the yarn tucked with different lengths in the experiment

Table 4 The simulation and experimental data of the yarn tucked in.

Length of yarn (mm)	Oblique-blowing simulation time (ms)	Average experimental time of oblique-blowing (ms)	Folding-in simulation time (ms)	Average experimental time of folding-in (ms)	Total time of numerical simulation (ms)	Average total experimental time (ms)	Final length of yarn in simulation (mm)	Final length of yarn in experiment (mm)
8	1.75	1.638	1.325	1.482	3.075	3.120	8.564	8.2
10	3.00	2.856	1.875	1.979	4.875	4.835	10.523	10.3
12	5.00	5.347	2.750	2.624	7.750	7.971	14.126	13.8
15	9.00	9.258	5.125	5.191	14.125	14.449	18.257	17.5

5. Conclusion

In this paper, the influence of yarn length on the yarn tucking in is studied and analysed through numerical simulation and visual experiment. The three-dimensional model of pneumatic tucked-in selvedge apparatus is established. On this basis, the numerical model of

airflow field and the finite element model of yarn are established, and their grid independence is verified. In order to draw a reliable conclusion and better explore the influence of the yarn length on the yarn spatial motion, a visual experimental platform was designed and established, and the state of yarns with different lengths during tucking-in was recorded by a high-speed camera. Combined with the numerical simulation and the experiment of yarn motion state and yarn motion trajectory at each point, the following conclusions can be drawn:

1. It is shown that the model proposed based on the one-way fluid–structure weak interaction algorithm can simulate the spatial motion of the yarn in the aerodynamically tucked in airflow field.
2. The longer the length of the yarn, the longer it takes for the yarn to be completely tucked in. When the length of the yarn reaches a certain level, the yarn will fail to be completely tucked in because the airflow cannot blow the yarn end.
3. When the yarn is too short, the force exerted on it by the folding-in airflow cannot resist the rebound force caused by the bending stiffness of the yarn, which will lead to an increase in the difficulty and failure rate of tucking-in.
4. After the yarn has been completely tucked in, the length of the yarn will increase, and the longer the yarn, the greater its elongation.

ACKNOWLEDGEMENTS

The authors gratefully acknowledge the support of the Zhejiang Provincial Natural Science Foundation of China (Grant No. LY18E050018).

REFERENCES

[1] De Meulemeester S., Githaiga J., Van Langenhove L., Hung D. V., Puissant P. Simulation of the Dynamic Yarn Behavior on Airjet Looms. Textile Research Journal, 2016, 75(10): 724-730. https://doi.org/10.1177/0040517505053950

[2] Delcour L, Peeters J, Degroote J. Three-dimensional fluid-structure interaction simulations of a yarn subjected to the main nozzle flow of an air-jet weaving loom using a Chimera technique. Textile Research Journal, 2020, 90(2): 194-212. https://doi.org/10.1177/0040517519862884

[3] Guo H. F., Chen Z. Y., Yu C. W. Numerical study of an air-jet spinning nozzle with a slotting-tube. Journal of Physics: Conference Series, 2011, 54(21-22): 4570-4579.

[4] Shih Tsan Hsing, Liou William W., Shabbir Aamir, Yang Zhigang, Zhu Jiang %J Computers Fluids. A New κ-ε Eddy Viscosity Model for High Reynolds Number Turbulent Flows, 1995, 24(3): 227-238. Textile Research Journal, 2020, 90(2): 194-212. https://doi.org/10.1016/0045-7930(94)00032-T

[5] Ahmed Hassan A. H., Afify Rola S., Hassanin Ahmed H., El-Hawary Ibrahim A., Mashaly Raafat I. Numerical and experimental study of the influence of nozzle flow parameters on yarn production by jet-ring spinning. Alexandria Engineering Journal, 2018, 57(4): 2975-2989. https://doi.org/10.1016/j.aej.2018.06.002

[6] Osman Akil, Delcour Lucas, Hertens Ine, Vierendeels Jan, Degroote Joris. Toward three-dimensional modeling of the interaction between the air flow and a clamped-free yarn inside the main nozzle of an air jet loom. Textile Research Journal, 2018, 89(6): 914-925. https://doi.org/10.1177/0040517518758006

[7] Tian F. B., Luo H., Zhu L., Liao J. C., Lu X. Y. An efficient immersed boundary-lattice Boltzmann method for the hydrodynamic interaction of elastic filaments. J Comput Phys, 2011, 230(19): 7266-7283. https://doi.org/10.1016/j.jcp.2011.05.028

[8] Jingyu Cui, Zhe Lin, Yuzhen Jin, Yang Liu. Numerical simulation of fiber conveyance in a confined channel by the immersed boundary-lattice Boltzmann method. European Journal of Mechanics - B/Fluids, 2019, 76: 422-433. https://doi.org/10.1016/j.euromechflu.2019.04.010

[9] Li Z, Shang Z, Zappa E, Van Langenhove L, Malengier B. Yarn level finite element method simulation for bending over sheaves of braided ropes. Journal of Industrial Textiles. 2023;53:122-131. https://doi.org/10.1177/15280837231189891

[10] Deng W, Wang X, Ke W, et al. Parametric 3D simulations of spun yarns and fabrics. The Journal of The Textile Institute, 2023: 1-10. https://doi.org/10.1080/00405000.2023.2230326

[11] Jonathan M. Kaldor,Doug L. James,Steve Marschner. Simulating knitted cloth at the yarn level. ACM Transactions on Graphics (TOG),2008,27(3):65.1-65.9. https://doi.org/10.1145/1360612.1360664

[12] Grzegorz Kondora,Dariusz Asendrych. Modelling the Dynamics of Flexible and Rigid Fibres. Chemical and Process Engineering,2013,34(1): 87-100. https://doi.org/10.2478/cpe-2013-0008

[13] Yingjie Zhou,Zhenyu Wu,Yisheng Liu,Zhong Xiang,Xudong Hu. Numerical and experimental study on the joint forming mechanism in the pneumatic splicing process. Textile Research Journal,2019,89(21-22): 4512-4525. https://doi.org/10.1177/0040517519837731

[14] Petrović J, Stamenković Ž, Bogdanović-Jovanović J, et al. Electro-Magnetoconvection of Conductive Immiscible Pure Fluid and Nanofluid. Transactions of FAMENA, 2022, 46(3): 13-28. https://doi.org/10.21278/TOF.463036021

[15] Sengottaiyan K, Swaminathan M R, Vencent C A, et al. Spray Characteristics of a Rotating Fuel Injector in a Direct Injection Diesel Engine. Transactions of FAMENA, 2023, 47(2): 13-29. https://doi.org/10.21278/TOF.472035621

[16] Ahmed H A H, Afify R S, Hassanin A H, et al. Numerical and experimental study of the influence of nozzle flow parameters on yarn production by jet-ring spinning. Alexandria engineering journal, 2018, 57(4): 2975-2989. https://doi.org/10.1016/j.aej.2018.06.002

[17] Osman A, Delcour L, Hertens I, et al. Toward three-dimensional modeling of the interaction between the air flow and a clamped-free yarn inside the main nozzle of an air jet loom. Textile Research Journal, 2019, 89(6): 914-925. https://doi.org/10.1177/0040517518758006

[18] Shanley K T, Ahmadi G, Hopke P K, et al. Simulated airflow and rigid fiber behavior in a realistic nasal airway model. Particulate Science and Technology, 2018, 36(2): 131-140. https://doi.org/10.1080/02726351.2016.1208694

[19] Rong Yin. Mathematical modeling and numerical simulation of nonlinearly elastic yarn in ring spinning. Textile Research Journal,2020,91(3-4): 278-288. https://doi.org/10.1177/0040517520940807

[20] Kim H A, Kim S J. Mechanical properties of micro modal air vortex yarns and the tactile wear comfort of knitted fabrics. Fibers and Polymers, 2018, 19(1): 211-218. https://doi.org/10.1007/s12221-018-7690-x

[21] Alexander Grechukhin, Pavel Rudovskiy, Galina Sokova, Andrey Korabelnikov. Carbon fabric 3D modeling according to nonlinear bending theory. The Journal of The Textile Institute 2020; 111(10): 1511-1517. https://doi.org/10.1080/00405000.2019.1707935

[22] Čarija Z, Mrša Z, Fućak S. Validation of Francis water turbine CFD simulations. Strojarstvo: časopis za teoriju i praksu u strojarstvu, 2008, 50(1): 5-14.

[23] Žic E, Černeka P, Biluš I. Hydrodynamic analysis of fluid obstruction around different geometric bodies. International Journal for Engineering Modelling, 2020, 33(1-2 Regular Issue): 59-77. https://doi.org/10.31534/engmod.2020.1-2.ri.05m

[24] Vinoth Kumar H, Sivakumar A. Integrating ergonomic factors with waste identification diagram to enhance operator performance and productivity in the textile industry. Transactions of FAMENA, 2022, 46(1): 1-21. https://doi.org/10.21278/TOF.461032621

[25] Damien André, Ivan Iordanoff, Jean-luc Charles, et al. Discrete element method to simulate continuous material by using the cohesive beam model. Computer Methods in Applied Mechanics and Engineering 2012;213-216: 113-125. https://doi.org/10.1016/j.cma.2011.12.002

[26] Liu Z, Zhang Z-L, Zhou C-Y, et al. An Adaptive Inverse-Distance Weighting Interpolation Method Considering Spatial Differentiation in 3D Geological Modeling. Geosciences 2021 ; 11(2): 1-18. https://doi.org/10.3390/geosciences11020051

[27] Hao X, Zeng Y. A review on the studies of air flow field and fiber formation process during melt blowing. Industrial & Engineering Chemistry Research, 2019, 58(27): 11624-11637. https://doi.org/10.1021/acs.iecr.9b01694

[28] Zhou S, Liu J, Wang Z, et al. Research on Design Optimization and Simulation of Regenerative Braking Control Strategy for Pure Electric Vehicle Based on EMB Systems. Transactions of FAMENA, 2023, 47(4): 33-49. https://doi.org/10.21278/TOF.474045522

[29] Hidetoshi Takeuchi, Nobuyuki Shimizu. An MBD approach for a simplified yarn model. Journal of Mechanical Science and Technology 2015;29(7): 2623-2629. https://doi.org/10.1007/s12206-015-0507-1

[30] Su N, Zhou Z J, Zhang Q, et al. Fault Feature Extraction of Bearings for the Petrochemical Industry and Diagnosis Based on High-Value Dimensionless Features. Transactions of FAMENA, 2022, 46(4): 31-44. https://doi.org/10.21278/TOF.464036521

Submitted: 23.11.2023

Accepted: 21.5.2024

Prof. Yisheng Liu*
Shuqi Zhou
Xufeng Sun
School of Mechanical Engineering,
Zhejiang Sci-Tech University, 310018
Zhejiang Hangzhou, China
*Corresponding author:
lysleo@zstu.edu.cn